Intelligent Control and Metaheuristic Optimization for Renewable-based Fast EV Charging Stations

FOUAD ZARO
Electrical Engineering Department,
Palestine Polytechnic University,
Hebron City,
PALESTINE

Abstract: - Fast-charging stations supplied by photovoltaic (PV) generation must regulate a common DC bus against intermittent generation and large, rapidly varying charging loads. This paper develops and analyses a grid-connected PV fast-charging station rated 1.755 MW, with a 1000 V DC bus, seven 80 kW chargers and a bidirectional three-level neutral-point-clamped grid converter. The station is described by an averaged dynamic model, formulated as an index-one differential-algebraic system with 47 states, from which the operating limits imposed by the system parameters are derived. The tuning of the proportional–integral (PI) controllers is stated as a constrained optimization problem with a time-weighted error cost, trajectory and stability constraints, and an existence argument for the optimal gains. The problem is solved with a Genetic Algorithm (GA), Particle Swarm Optimization (PSO) and the Grey Wolf Optimizer (GWO) under an identical evaluation budget. Perturb and Observe (P&O) and Incremental Conductance (INC) maximum power point tracking (MPPT) are compared on a 650 W module. Both achieve tracking efficiencies above 99.6 % and recover from irradiance steps within 3 ms, while INC removes the steady-state power oscillation of P&O (1.2 W peak-to-peak at 1000 W/m²). In the tuning runs, PSO and GWO reached the same best fitness within five iterations, whereas GA converged more slowly and ended 0.08 % higher after 50 generations.

Key-Words: - Electric vehicle fast charging; photovoltaic systems; differential-algebraic model; PI controller tuning; metaheuristic optimization; Grey Wolf Optimizer; maximum power point tracking; incremental conductance.

Received: April 25, 2026. Revised: June 27, 2026. Accepted: July 29, 2026. Published: November 23, 2026.

1 Introduction

The transition from fossil fuels to renewable energy is accelerating in response to climate change and sustainability goals, and the electrification of transport is a central part of this transition [1]. Photovoltaic (PV) systems are widely adopted because they generate clean, decentralized electricity. However, their intermittency poses challenges for applications that require high reliability, such as electric vehicle (EV) charging stations [2].

Large-scale EV deployment demands a robust fast-charging infrastructure [3]. Conventional grid-connected fast-charging stations draw large, rapidly varying power, which causes voltage fluctuations, harmonic distortion and peak-demand stress in the distribution network [4]. Integrating renewable generation into the charging station reduces these impacts, lowers operating costs and decentralizes the energy supply [1], [2].

In PV-powered stations, efficient energy extraction requires Maximum Power Point Tracking (MPPT). Perturb and Observe (P&O) and Incremental Conductance (INC) are the most widely used MPPT algorithms, but their behaviour differs under changing irradiance and load conditions [5]. Regulation of the DC-bus voltage is equally critical. Proportional–integral (PI) controllers are commonly used, but their performance depends strongly on parameter tuning, and conventional tuning methods often result in overshoot, long settling times or poor robustness [6]. Metaheuristic optimization techniques, including the Genetic Algorithm (GA), Particle Swarm Optimization (PSO) and the Grey Wolf Optimizer (GWO), have shown promise in tuning such controllers for grid-connected PV converters [6], [7].

This study models, tunes and evaluates a PV-based fast-charging station with a 1000 V DC bus, seven 80 kW chargers and a bidirectional grid interface. The main contributions are:

- A complete averaged dynamic model of the station, formulated as a differential-algebraic system, including the PV arrays, boost

converters, chargers, battery, DC link, grid converter and PLL, together with the operating limits imposed by the system parameters.

- A formal constrained optimization problem for tuning the PI gains of the station, with an explicit cost function, constraints and an existence argument for the optimal solution.
- A comparison of P&O and INC MPPT on a common benchmark, and of the convergence of GA, PSO and GWO on the tuning problem under an identical computational budget.

The rest of the paper is organized as follows. Section 2 presents the system model, Section 3 the MPPT algorithms, Section 4 the optimization problem and the metaheuristic algorithms, Section 5 the simulation results, and Section 6 the conclusions.

The proposed EV charging station employs a multilayer control architecture comprising three main units, as shown in Figure 1:

1 DC–DC converter control: implements MPPT to maximize PV power extraction through the boost converters.
2 Grid-converter control: DC-link voltage regulation, current control, grid synchronization, and active and reactive power control.
3 EV charger control: Constant Current (CC) and Constant Voltage (CV) charging according to the battery state of charge (SoC).

The DC–DC converter serves as the interface between the PV array and the DC bus. An MPPT algorithm continuously tracks the optimal operating point under varying environmental conditions. The controller adjusts the boost converter duty cycle to maximize energy extraction, thereby enhancing efficiency and reducing grid dependency.

The station comprises two PV farms with a combined DC rating of 1.755 MW, built from 650 W mono-crystalline modules arranged in strings of 20 (string Vmp = 758 V). Farm 1 contains 77 strings (1.00 MW) and Farm 2 contains 58 strings (0.754 MW), for 2,700 modules in total. Each farm is connected to the 1000 V DC bus through a boost converter under MPPT control, which operates at a duty cycle of about 0.24 at standard test conditions. Seven 80 kW DC fast chargers are supplied from the DC bus, giving a maximum charging demand of 560 kW. The PV rating was derived from the station's estimated daily demand of 7,007 kWh/day, obtained from a HOMER-based techno-economic sizing of the station [8], so under high irradiance the plant supplies the full charging load and exports the surplus to the 11 kV grid through a 2.25 MVA three-level NPC converter and a 0.5/11 kV step-up transformer. The main system parameters are listed in Table 1 (Appendix).

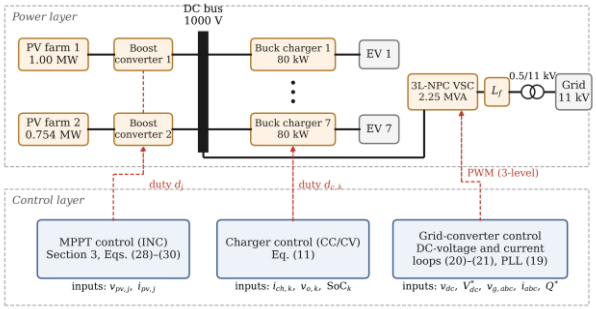

Fig. 1: Comprehensive Control Architecture of the Proposed Electric Vehicle Charging Station
Source: created by the author

2 System Modelling

This section develops the averaged dynamic model of the charging station shown in Figure 1. Each converter is represented by its state-space model averaged over one switching period. This is valid because the switching frequencies (Table 1, Appendix) are at least two orders of magnitude above the bandwidth of the control loops. The subsystem models are then assembled into a single set of differential-algebraic equations (DAE), which is the basis of the stability analysis and the controller optimization in the following sections. The parameter values are listed in Table 1 (Appendix) and the operating limits they impose are summarized in Table 2.

2.1 PV Array Model

Each PV farm consists of N_p parallel strings of N_s series-connected modules, each module containing N_c series cells. Using the single-diode model [9], the terminal current i and voltage v of an array satisfy the implicit relation

$$i = N_p I_{ph} - N_p I_0 \left[\exp\left(\frac{v + iR_s'}{nN_cN_sV_T}\right) - 1\right] - \frac{v + iR_s'}{R_{sh}'} \quad (1)$$

where $R_s' = R_sN_s/N_p$ and $R_{sh}' = R_{sh}N_s/N_p$ are the array-equivalent series and shunt resistances, n is the diode ideality factor, and $V_T = kT/q$ is the thermal voltage. The photocurrent and saturation current depend on irradiance G and cell temperature T as

$$I_{ph} = \left[I_{ph,\mathrm{STC}} + K_I\,(T - T_{\mathrm{STC}})\right]\frac{G}{G_{\mathrm{STC}}} \quad (2)$$

$$I_0 = I_{0,\mathrm{STC}} \left(\frac{T}{T_{\mathrm{STC}}}\right)^3 \exp\left[\frac{qE_g}{nk}\left(\frac{1}{T_{\mathrm{STC}}} - \frac{1}{T}\right)\right] \quad (3)$$

where K_I is the temperature coefficient of the short-circuit current and E_g is the band-gap energy. The module parameters were fitted to the datasheet values of Table 1 (Appendix) by matching the short-circuit, open-circuit and maximum power points together with the condition $dp/dv = 0$ at the MPP, which gives $N_c = 66$, $n = 1.05$, $I_{ph,\mathrm{STC}} = 18.41$ A, $I_{0,\mathrm{STC}} = 1.89 \times 10^{-10}$ A, $R_s = 0.094\ \Omega$ and $R_{sh} = 92.8\ \Omega$. With these values the model reproduces $P_{mp} = 650.4$ W at $V_{mp} = 37.9$ V.

The array power is $p = v\,i$. At the maximum power point

$$\frac{dp}{dv} = i + v\,\frac{di}{dv} = 0 \quad \Leftrightarrow \quad \frac{di}{dv} = -\frac{i}{v} \quad (4)$$

Differentiating (1) implicitly gives the incremental conductance in closed form:

$$\begin{aligned} \frac{di}{dv} &= -\frac{g_d + {G_{sh}}'}{1 + {R_s}'\,(g_d + {G_{sh}}')} \\ g_d &= \frac{N_p I_0}{n N_c N_s V_T} \exp\left(\frac{v + i{R_s}'}{n N_c N_s V_T}\right) \end{aligned} \quad (5)$$

where ${G_{sh}}' = 1/{R_{sh}}'$. Because g_d increases monotonically with v, the P–V curve under uniform irradiance has a single maximum. The INC algorithm uses the sign of $di/dv + i/v$ to locate it:

$$\frac{di}{dv} + \frac{i}{v} \begin{cases} > 0, & v < V_{mp}\text{: increase } v \\ = 0, & v = V_{mp}\text{: hold } v \\ < 0, & v > V_{mp}\text{: decrease } v \end{cases} \quad (6)$$

In the implementation, the hold condition is replaced by the tolerance band $|di/dv + i/v| \le \varepsilon\, i/v$, which removes the steady-state oscillation of the operating point.

2.2 Boost Converter Model

Each PV farm $j \in \{1,2\}$ is connected to the DC bus through a boost converter with input capacitor C_{in}, inductor L_b (resistance r_L) and duty cycle d_j. In continuous conduction mode, the averaged model is

$$C_{in}\,\frac{dv_{pv,j}}{dt} = i_{pv,j} - i_{L,j} \quad (7)$$

$$L_b\,\frac{di_{L,j}}{dt} = v_{pv,j} - \left(1 - d_j\right) v_{dc} - r_L\, i_{L,j} \quad (8)$$

and the current injected into the DC bus is $i_{b,j} = \left(1 - d_j\right) i_{L,j}$. In steady state, (8) gives $V_{dc} = V_{pv,j}/\left(1 - D_j\right)$ (neglecting r_L). The MPPT algorithm therefore sets the PV operating voltage through the duty cycle, $V_{pv,j} = \left(1 - D_j\right) V_{dc}$.

2.3 EV Charger Model

Each charger $k = 1, \ldots, N_{ev}$ ($N_{ev} = 7$) is a buck converter [10] with inductor L_c (resistance r_c), output capacitor C_o and duty cycle $d_{c,k}$:

$$L_c\,\frac{di_{c,k}}{dt} = d_{c,k}\, v_{dc} - v_{o,k} - r_c\, i_{c,k} \quad (9)$$

$$C_o\,\frac{dv_{o,k}}{dt} = i_{c,k} - i_{ch,k} \quad (10)$$

where $i_{ch,k}$ is the charging current delivered to the battery. The charger draws $d_{c,k}\, i_{c,k}$ from the DC bus. The CC/CV strategy [11] switches the regulated quantity according to the state of charge:

$$d_{c,k} = \begin{cases} \mathrm{PI}_c\left(I_{CC} - i_{ch,k}\right), & \mathrm{SoC}_k < 0.8 \ \text{CC mod} \\ \mathrm{PI}_c\left(V_{CV} - v_{o,k}\right), & \mathrm{SoC}_k \ge 0.8 \ \text{CV mod} \end{cases} \quad (11)$$

with $I_{CC} = 100$ A and $V_{CV} = 830$ V. Here $\mathrm{PI}(e) = K_p e + K_i \int_0^t e\ d\tau$.

2.4 EV Battery Model

The EV battery is represented by the Li-ion dynamic model of Tremblay and Dessaint, which is the model implemented in the MATLAB/Simulink battery block [12]. Using the discharge-positive current convention $i_{b,k} = -i_{ch,k}$, the terminal voltage in charge mode ($i^*_{b,k} < 0$) is

$$\begin{aligned} v_{o,k} = \ & E_0 - R_b\, i_{b,k} - K\,\frac{Q}{q_{e,k} + 0.1Q}\, i^*_{b,k} \\ & - K\,\frac{Q}{Q - q_{e,k}}\, q_{e,k} + A\, e^{-B q_{e,k}} \end{aligned} \quad (12)$$

where E_0 is the constant voltage, R_b the internal resistance, K the polarization constant, Q the capacity (62.5 Ah), and A, B the exponential-zone parameters. The extracted charge $q_{e,k}$ (Ah) and the filtered current $i^*_{b,k}$ evolve as

$$\begin{aligned} \frac{dq_{e,k}}{dt} &= \frac{i_{b,k}}{3600} \\ \tau_b\,\frac{di^*_{b,k}}{dt} &= i_{b,k} - i^*_{b,k} \\ \mathrm{SoC}_k &= 1 - \frac{q_{e,k}}{Q} \end{aligned} \quad (13)$$

The polarization terms in (12) act as an SoC-dependent internal resistance. The filtered current $i^*_{b,k}$ plays the role of the RC branch of a first-order Thevenin equivalent circuit, with time constant τ_b.

2.5 DC-Link Model

The DC link of the three-level NPC converter consists of two series capacitors $C_1 = C_2$, giving $C_{eq} = C_1 C_2/(C_1 + C_2) = 75$ µF. The neutral point

is assumed balanced. Kirchhoff's current law at the DC bus gives

$$C_{eq}\frac{dv_{dc}}{dt} = \sum_{j=1}^{2}(1-d_j)\,i_{L,j} - \sum_{k=1}^{N_{ev}} d_{c,k}\,i_{c,k} - i_{inv} \quad (14)$$

where i_{inv} is the DC-side current of the grid converter. Multiplying (14) by v_{dc} gives the energy balance of the DC link:

$$C_{eq}\,v_{dc}\frac{dv_{dc}}{dt} = \frac{d}{dt}\left(\frac{1}{2}C_{eq}v_{dc}^2\right) = P_{PV} - P_{EV} - P_{grid} - P_{loss} \quad (15)$$

where P_{PV} is the power delivered by the two boost converters, P_{EV} the total charging power, P_{grid} the power exported to the grid, and P_{loss} the conversion losses. Because the stored energy is only $1/2\,C_{eq}V_{dc}^2 = 37.5$ J (about 21 µs of rated PV power), any power imbalance appears almost immediately as a DC-voltage deviation. This is why the DC-voltage regulator of the grid converter is the key loop for the stability of the station.

2.6 Grid-Side Converter and PLL Model

The grid-side converter, a three-level NPC voltage-source converter [13], is connected to the 11 kV grid through the filter (L_f, R_f) and a 0.5/11 kV transformer, whose leakage impedance is referred to the low-voltage side and lumped into (L_f, R_f). In a reference frame rotating at the grid angular frequency ω (amplitude-invariant Park transformation), the filter dynamics are

$$L_f\frac{di_d}{dt} = v_{cd} - v_{gd} - R_f\,i_d + \omega L_f\,i_q \quad (16)$$

$$L_f\frac{di_q}{dt} = v_{cq} - v_{gq} - R_f\,i_q - \omega L_f\,i_d \quad (17)$$

where $v_{c,dq}$ are the converter output voltages, $v_{g,dq}$ the grid voltages at the point of common coupling, and i_{dq} the currents injected into the grid. The powers exchanged with the grid are

$$P_{grid} = \frac{3}{2}\left(v_{gd}\,i_d + v_{gq}\,i_q\right), \quad Q_{grid} = \frac{3}{2}\left(v_{gq}\,i_d - v_{gd}\,i_q\right) \quad (18)$$

For the averaged converter, power conservation gives $v_{dc}\,i_{inv} = 3/2\,(v_{cd}\,i_d + v_{cq}\,i_q)$, which couples (14) to (16)–(17). The converter voltages are produced by the modulator as $v_{c,dq} = m_{dq}\,v_{dc}/2$, where m_{dq} are the modulation indices.

Grid synchronization uses a synchronous-reference-frame PLL [14] that drives v_{gq} to zero:

$$\frac{d\theta}{dt} = \omega_0 + K_{p,pll}\,v_{gq} + K_{i,pll}\,\xi_{pll}, \quad \frac{d\xi_{pll}}{dt} = v_{gq}, \quad v_{gq} = -V_g\sin(\theta-\theta_g) \quad (19)$$

where $\omega_0 = 2\pi\cdot 50$ rad/s and θ_g and V_g are the grid voltage angle and amplitude. When the PLL is locked ($v_{gq}=0$, $v_{gd}=V_g$), (18) reduces to $P_{grid} = 3/2\,V_g\,i_d$ and $Q_{grid} = -3/2\,V_g\,i_q$, so i_d controls the active power and i_q the reactive power independently.

The cascaded controller, shown in Figure 2 [14], consists of an outer DC-voltage loop and inner decoupled current loops:

$$i_d^* = K_{p,v}\,(v_{dc} - V_{dc}^*) + K_{i,v}\,\xi_v, \quad \frac{d\xi_v}{dt} = v_{dc} - V_{dc}^* \quad (20)$$

$$v_{cd}^* = v_{gd} - \omega L_f\,i_q + K_{p,i}\,(i_d^* - i_d) + K_{i,i}, \quad v_{cq}^* = v_{gq} + \omega L_f\,i_d + K_{p,i}\,(i_q^* - i_q) + K_{i,i} \quad (21)$$

with $\dot{\xi}_d = i_d^* - i_d$ and $\dot{\xi}_q = i_q^* - i_q$. The reactive-power reference is $i_q^* = -2Q^*/(3V_g)$, with $Q^* = 0$ (unity power factor). With the feed-forward and decoupling terms in (21), the closed current loops reduce to $L_f\,di_{dq}/dt = -R_f\,i_{dq} + K_{p,i}(i_{dq}^* - i_{dq}) + K_{i,i}\,\xi_{dq}$, which is linear and decoupled.

The control loops diagram for the study shown in Figure 2.

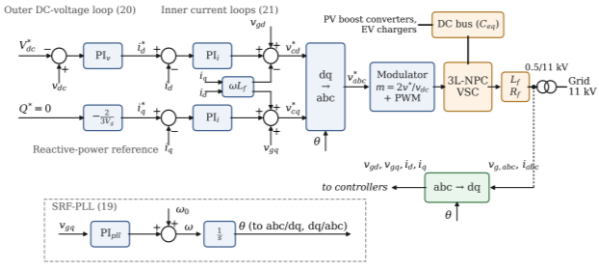

Fig. 2: Voltage Source Converter (VSC) inner and outer control loop diagram for the study.
Source: created by the author

2.7 Complete System as a Differential-Algebraic Model

Collecting (1) – (21), the charging station is described by the semi-explicit DAE

$$\dot{\mathbf{x}} = \mathbf{f}(\mathbf{x},\mathbf{z},\mathbf{u},\mathbf{w}), \quad \mathbf{0} = \mathbf{g}(\mathbf{x},\mathbf{z},\mathbf{w}), \quad \mathbf{u} = \boldsymbol{\kappa}(\mathbf{x},\mathbf{z};\boldsymbol{\theta}) \quad (22)$$

with the state, algebraic, input and disturbance vectors

$$\begin{aligned} \mathbf{x} &= \left[\mathbf{x}_{pv}^T,\ v_{dc},\ \mathbf{x}_g^T,\ \mathbf{x}_{ev,1}^T,\ \ldots,\ \mathbf{x}_{ev,N_{ev}}^T\right] \\ \mathbf{x}_{pv} &= \left[v_{pv,1},\ v_{pv,2},\ i_{L,1},\ i_{L,2}\right]^T \\ \mathbf{x}_g &= \left[i_d,\ i_q,\ \theta,\ \xi_{pll},\ \xi_v,\ \xi_d,\ \xi_q\right]^T \\ \mathbf{x}_{ev,k} &= \left[i_{c,k},\ v_{o,k},\ q_{e,k},\ i_{b,k}^*,\ \xi_{c,k}\right]^T \end{aligned} \quad (23)$$

$$\begin{aligned} \mathbf{z} &= \left[i_{pv,j},\ P_{grid},\ Q_{grid}\right]^T \\ \mathbf{u} &= \left[d_j,\ d_{c,k},\ m_d,\ m_q\right]^T \\ \mathbf{w} &= \left[G,\ T,\ V_g,\ \theta_g\right]^T \end{aligned} \quad (24)$$

for $j = 1,2$ and $k = 1, \ldots, N_{ev}$, so that $\dim\mathbf{x} = 4 + 1 + 7 + 5N_{ev} = 47$. The function $\mathbf{f}$ collects (7) – (10), (13), (14), (16), (17) and the integrator dynamics of (11), (19) – (21). The function $\mathbf{g}$ collects the implicit PV equation (1) for each farm and the power relations (18); the battery voltage (12) is an explicit output of the states. The control law $\boldsymbol{\kappa}$ contains the MPPT, CC/CV and grid-converter controllers and is parameterized by the vector of PI gains

$$\boldsymbol{\theta} = \left[K_{p,v},\ K_{i,v},\ K_{p,i},\ K_{i,i},\ K_{p,c},\ K_{i,c}\right]^T \quad (25)$$

which is the decision variable of the metaheuristic optimization in Section 4.

Well-posedness. The algebraic equations have a non-singular Jacobian with respect to $\mathbf{z}$. For the PV equation (1), writing it as $g_{pv}(v, i) = 0$,

$$\frac{\partial g_{pv}}{\partial i} = -1 - R_s'\,(g_d + G_{sh}') \le -1 < 0 \quad (26)$$

for all operating points, and (18) is explicit in P_{grid} and Q_{grid}. The DAE (22) is therefore of index one. By the implicit function theorem, $\mathbf{z} = \mathbf{h}(\mathbf{x}, \mathbf{w})$ exists locally and is unique and continuously differentiable, so (22) reduces to the ODE $\dot{\mathbf{x}} = \mathbf{f}(\mathbf{x}, \mathbf{h}(\mathbf{x}, \mathbf{w}), \boldsymbol{\kappa}(\mathbf{x}, \mathbf{h}; \boldsymbol{\theta}), \mathbf{w})$. Because $\mathbf{f}$ is continuously differentiable within each operating mode (fixed MPPT duty cycle between updates, and CC or CV charging), it is locally Lipschitz. By the Picard–Lindelöf theorem, the solution exists and is unique on every interval between mode transitions. The MPPT updates and CC→CV transitions are discrete events at which the state is continuous, so the overall trajectory is well defined as the concatenation of these solutions.

2.8 Operating Limits

The parameters of Table 1 (Appendix) bound the admissible operating region of the station. These bounds are summarized in Table 2 and enter the optimization problem of Section 4 as constraints.

Table 2. Operating limits imposed by the system parameters

No.	Limit	Expression	Value
1	Boost duty cycle at MPP	$D_j = 1 - V_{mp,str}(T)/V_{dc}$	$0.18 \le D_j \le 0.33$ ($T = -5$ to 70 °C)
2	PV string voltage	$V_{oc,str}(T_{min}) \le V_{sys,max}$	970 V ≤ 1500 V
3	PV farm current	$i_{pv,j} \le N_p I_{sc}$	1416 A (farm 1); 1067 A (farm 2)
4	Buck duty cycle / DC-bus headroom	$d_{c,k} = v_{o,k}/v_{dc} < 1$	$d_{c,k} \le 0.83$; requires $v_{dc} >$ 830 V
5	NPC linear modulation	$v_{dc} \ge 2\sqrt{2}\,V_{LL}/\sqrt{3}$	$v_{dc} \ge 816$ V (m = 0.82 at 1000 V)
6	Grid-converter current	$I_g \le S_n/(\sqrt{3}\,V_{LL})$	2598 A (rms)
7	Charging current / C-rate	$i_{ch,k} \le I_{CC}$; $C = I_{CC}/Q$	100 A; 1.6C
8	Battery terminal voltage	$v_{o,k} \le V_{CV}$	830 V
9	Charging demand vs. converter rating	$N_{ev}P_{ch} \le S_n$	560 kW ≤ 2.25 MVA
10	Filter reactance	$X_f = \omega L_f/Z_{base}$	0.125 pu
11	DC-link stored energy	$E_{dc} = \frac{1}{2}C_{eq}V_{dc}^2$	37.5 J (≈ 21 µs at 1.755 MW)

Source: created by the author

Constraints 4 and 5 together bound the DC-bus voltage from below. The buck chargers need $v_{dc} > V_{CV} = 830$ V to regulate the battery voltage in CV mode, and the NPC converter needs $v_{dc} \ge 816$ V to remain in the linear modulation range. A transient DC-voltage dip of more than about 17 % below the 1000 V reference would therefore saturate the chargers and push the grid converter into over-modulation. The maximum transient deviation of v_{dc} is thus a hard constraint in the controller optimization. The small DC-link energy (constraint 11) means that such dips develop within milliseconds of a power imbalance, which is why the tuning of the DC-voltage loop (20) determines the dynamic performance of the whole station.

3 Maximum Power Point Tracking

Each PV farm is operated at its maximum power point by an MPPT algorithm that updates the boost-converter duty cycle d_j every T_m seconds. From (8), the PV operating voltage is set through the duty cycle as $V_{pv,j} = (1 - D_j)\,V_{dc}$, so increasing d_j lowers the PV voltage. Two widely used algorithms

are compared: Perturb and Observe (P&O) and Incremental Conductance (INC) [5],[15]. Both are written below in terms of the sampled PV voltage $V[k]$, current $I[k]$ and power $P[k] = V[k]\,I[k]$, with $\Delta V[k] = V[k] - V[k-1]$, $\Delta I[k] = I[k] - I[k-1]$, $\Delta P[k] = P[k] - P[k-1]$, and a fixed duty-cycle step Δd.

3.1 Perturb and Observe

P&O keeps moving the operating point in the direction that increased the power at the previous step and reverses otherwise:

$$d[k+1] = d[k] - \Delta d\ \mathrm{sgn}(\Delta P[k]\,\Delta V[k]) \quad (27)$$

The algorithm needs only one multiplication per step. However, it never stops perturbing, so in steady state the operating point oscillates around the MPP with an amplitude set by Δd. In addition, P&O cannot distinguish a power change caused by its own perturbation from one caused by a change in irradiance, which can move the operating point in the wrong direction during fast irradiance transients [5], [15].

3.2 Incremental Conductance

INC evaluates the MPP condition (4)–(6) directly from measured increments, replacing di/dv by $\Delta I/\Delta V$ in the indicator

$$g[k] = \frac{\Delta I[k]}{\Delta V[k]} + \frac{I[k]}{V[k]} \quad (28)$$

and updates the duty cycle as

$$d[k+1] = d[k] - \Delta d\ s[k] \quad (29)$$

with the step direction

$$s[k] = \begin{cases} \mathrm{sgn}(\Delta I[k]), & \Delta V[k] = 0 \\ \mathrm{sgn}(g[k]), & |g[k]| > \varepsilon\, I[k]/V[k] \\ 0, & \text{otherwise} \end{cases} \quad (30)$$

The tolerance ε defines a band around the MPP inside which the duty cycle is held constant, so INC does not oscillate once the MPP is reached. The case $\Delta V[k] = 0$ detects irradiance changes that occur while the operating voltage is held. The price is one division per step and a slightly more complex implementation than P&O [15].

3.3 Benchmark Set-Up and Performance Indices

Both algorithms were tested on a single 650 W module (Table 1, Appendix), modelled by (1) – (3) and connected to the averaged boost converter (7) – (8) with the output clamped at a constant voltage. This isolates the tracking behaviour from the dynamics of the rest of the station. The same step size and update period were used for both algorithms (Table 3). Two irradiance scenarios were applied at $T = 25$ °C: a constant 1000 W/m², and a step profile of 1000 → 800 → 700 W/m² at $t = 0.3$ s and $t = 0.6$ s (Figure 6). The algorithms are compared by the settling time to within ±2 % of P_{mpp}, the steady-state peak-to-peak power ripple ΔP_{pp}, and the tracking efficiency

$$\eta_{MPPT} = \frac{\int_0^{T_{sim}} P\,(t)\,dt}{\int_0^{T_{sim}} P_{mpp}\,(t)\,dt} \times 100\,\% \quad (31)$$

where $P_{mpp}(t)$ is the maximum power available at the instantaneous irradiance, computed from (1) – (3).

Table 3. MPPT benchmark settings (identical for P&O and INC)

Parameter	Value
PV module	650 W (Table 1, Appendix), T = 25 °C
Boost output voltage V_o	100 V (clamped)
Inductor L_b / resistance r_L	1 mH / 20 mΩ
Input capacitor C_{in}	220 µF
MPPT update period T_m	1 ms
Duty-cycle step Δd	0.004 (ΔV ≈ 0.4 V)
INC tolerance ε	0.10
Initial duty cycle d[0]	0.70
Integration step / simulated time	2 µs / 1 s (MATLAB)

Source: created by the author

The selected MPPT algorithm, INC, is applied with the same settings to both PV farms of the station in Section 5.

4 Controller Tuning by Metaheuristic Optimization

The station contains several PI loops whose gains, collected in the vector $\boldsymbol{\theta}$ of (25), interact through the DC link (14). A change in one loop alters the dynamics of all the others, so tuning each loop separately does not guarantee good overall behaviour. In this section, the tuning is formulated as a constrained optimization problem over the closed-loop model (22). The problem is then solved with three metaheuristic algorithms, GA, PSO and GWO [6], [7], under an identical computational budget.

4.1 Optimization Problem

Decision variables. The gains are restricted to the box

$$\Theta = \{\theta \in \mathbb{R}^{n_\theta} : \theta_{\min} \le \theta \le \theta_{\max}\} \quad (32)$$

where the inequalities hold component wise and $n_\theta = 6$

Cost function. Each candidate $\boldsymbol{\theta}$ is evaluated by simulating (22) over a tuning scenario of length T_f. The scenario contains an irradiance step from 1000 to 600 W/m² and the connection of the seven 80 kW chargers. The cost is the time-weighted absolute error (ITAE) of the regulated quantities, normalized by their references:

$$J(\theta) = \int_0^{T_f} t\,\frac{|e_v(t;\theta)|}{V_{dc}^*}\,dt + \frac{\lambda_c}{N_{ev}}\sum_{k=1}^{N_{ev}}\int_0^{T_f} t\,\frac{|e_{c,k}(t;\theta)|}{I_{CC}}\,dt \quad (33)$$

where $e_v = V_{dc}^* - v_{dc}$ is the DC-bus voltage error, $e_{c,k}$ is the error of charger k in its active CC or CV mode, and λ_c is a weighting factor ($\lambda_c = 1$). The time weighting t penalizes errors that persist, so ITAE favours well-damped responses with short settling times.

Constraints. The operating limits of Table 2 are imposed along the whole trajectory, together with a stability margin:

$$\begin{aligned} h_1(\theta) &= V_{\min} - \min_t v_{dc}(t;\theta) \le 0 \\ h_2(\theta) &= \max_t v_{dc}(t;\theta) - V_{\max} \le 0 \\ h_3(\theta) &= \max_t |i_g(t;\theta)| - \sqrt{2}\,I_{g,\max} \le 0 \\ h_4(\theta) &= \max_i \mathrm{Re}\,\lambda_i(\mathbf{A}_{cl}(\theta)) + \sigma_{\min} \le 0 \end{aligned} \quad (34)$$

where $V_{\min} = 830$ V and $I_{g,\max} = 2598$ A are taken from Table 2 (limits 4 – 6), $V_{\max} = 1.1\,V_{dc}^*$, $\mathbf{A}_{cl}(\boldsymbol{\theta})$ is the Jacobian of (22) linearized at the nominal operating point, and $\sigma_{\min} > 0$ is the required stability margin. The tuning problem is

$$\begin{aligned} \theta^* &= \arg\min_{\theta\in\Theta_f} J(\theta) \\ \Theta_f &= \{\theta \in \Theta : h_m(\theta) \le 0,\ m = 1,\dots,4\} \end{aligned} \quad (35)$$

The metaheuristics operate on the penalized fitness

$$F(\theta) = J(\theta) + \rho\sum_{m=1}^{4}[\max\{0,\ h_m(\theta)\}]^2 \quad (36)$$

with a penalty weight ρ large enough that every infeasible candidate has a higher fitness than every feasible one ($\rho = 10^3$). $F = J$ on Θ_f, so minimizing F over Θ solves (35).

Existence of an optimal solution. Θ is compact. Each h_m is continuous in $\boldsymbol{\theta}$: h_1–h_3 because the trajectories of (22) depend continuously on $\boldsymbol{\theta}$ (see below), and h_4 because the eigenvalues of a matrix are continuous functions of its entries. Θ_f is therefore closed and, as a subset of Θ, compact. It is non-empty provided that at least one gain vector in Θ satisfies the four constraints; the initial manually tuned gains, with which the station operates stably in simulation, are used as such a starting point.

Assume that, over the tuning scenario, the sequence of discrete events of (22) (MPPT updates and CC/CV transitions) does not change for $\boldsymbol{\theta} \in \Theta_f$. Then, between events, $\mathbf{f}$ is continuously differentiable in $(\mathbf{x}, \boldsymbol{\theta})$, and Gronwall's inequality shows that $\mathbf{x}(t;\boldsymbol{\theta})$ depends continuously on $\boldsymbol{\theta}$ uniformly on $[0, T_f]$. Hence J is continuous on the compact set Θ_f, and by the Weierstrass extreme value theorem a minimizer $\boldsymbol{\theta}^*$ of (35) exists. If the event sequence does change with $\boldsymbol{\theta}$, J may be discontinuous. In that case $J \ge 0$ still has a finite infimum on Θ_f, which the algorithms approximate.

Table 4. Settings of the optimization algorithms

Setting	Value
Population size N (all algorithms)	30
Iterations T_{max}	50
Fitness evaluations N × T_{max}	1500 per algorithm
Gain bounds θ_{min} / θ_{max}	0.1 θ_0 / 10 θ_0 (θ_0 = initial manually tuned gains)
Tuning scenario length T_f	0.5 s
GA: selection / crossover / mutation	Tournament (size 2); arithmetic, p_c = 0.8; Gaussian mutation, p_m = $1/n_\theta$, $\sigma_n = 0.1(\theta_{max,n} - \theta_{min,n})$; elitism 1
PSO: w / c_1 / c_2	0.729 / 1.494 / 1.494
GWO: convergence parameter a	Linear, 2 → 0, Eq. (45)
Penalty weight ρ	10^3
Stability margin σ_{min}	20 s^{-1}

Source: created by the author

Uniqueness and choice of solver. Uniqueness of $\boldsymbol{\theta}^*$ is not claimed. The closed-loop dynamics depend on products of gains and states, so J is in general nonconvex and may have several local minima. J is also available only through simulation, not in closed form, so gradient information cannot be obtained. These properties motivate derivative-free, population-based global search. The algorithms used are described in Sections 4.2 – 4.4, the complete

tuning procedure with GWO is shown in Figure 3, and the algorithms settings are given in Table 4.

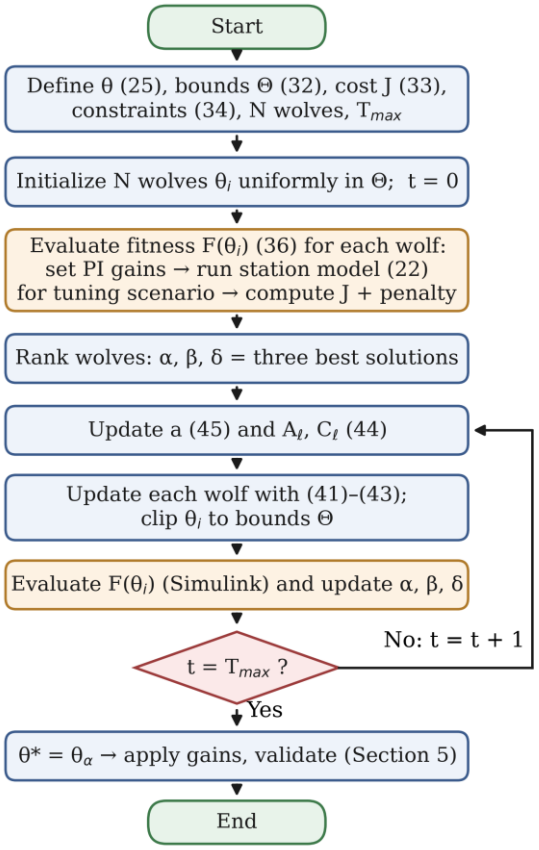

Fig. 3: Flowchart of the GWO-based tuning of the PI gains, with the station model (22) evaluated in the loop
Source: created by the author

4.2 Genetic Algorithm

The real-coded GA evolves a population of N candidate gain vectors through selection, crossover and mutation, with elitism preserving the best individual in each generation [16]. Parents $\boldsymbol{\theta}_a$, $\boldsymbol{\theta}_b$ are chosen by tournament selection and combined by arithmetic crossover:

$$\boldsymbol{\theta}_c = \mu\,\boldsymbol{\theta}_a + (1-\mu)\,\boldsymbol{\theta}_b, \qquad \mu \sim \mathcal{U}(0,1) \tag{37}$$

Each component of the offspring is then mutated with probability p_m:

$$\theta_{c,n} \leftarrow \theta_{c,n} + \sigma_n\,\mathcal{N}(0,1) \tag{38}$$

where σ_n is proportional to the width of the admissible interval of component n. For an elitist GA, the best solution converges in probability to the global optimum as the number of generations tends to infinity [16]. However, convergence is typically slow.

4.3 Particle Swarm Optimization

In PSO, each particle i has a position $\boldsymbol{\theta}_i$ and a velocity $\mathbf{v}_i$. Both are updated using the particle's best position $\mathbf{p}_i$ and the swarm's best position $\mathbf{g}$ [17]:

$$\mathbf{v}_i(t+1) = w\,\mathbf{v}_i(t) + c_1\mathbf{r}_1 \circ \big(\mathbf{p}_i - \boldsymbol{\theta}_i(+ c_2\mathbf{r}_2 \circ \big(\mathbf{g} - \boldsymbol{\theta}_i(t)\big) \tag{39}$$

$$\boldsymbol{\theta}_i(t+1) = \boldsymbol{\theta}_i(t) + \mathbf{v}_i(t+1) \tag{40}$$

where w is the inertia weight, c_1 and c_2 are the acceleration coefficients, $\mathbf{r}_1, \mathbf{r}_2 \sim \mathcal{U}(0,1)^{n_\theta}$, and $\circ$ denotes element-wise multiplication. For parameters inside the stability region discussed in [17], the particle trajectories converge. Convergence to the global optimum is not guaranteed, and premature stagnation in a local minimum is the main weakness of PSO [17]. PSO has nevertheless been applied successfully to power-system planning problems such as the optimal sizing and placement of distributed generators [18].

4.4 Grey Wolf Optimizer

GWO imitates the leadership hierarchy and hunting behaviour of grey wolves [19]. It has been widely applied in energy systems [20], including the tuning of controllers for grid-connected PV inverters [7]. The three best solutions found so far are designated alpha (α), beta (β) and delta (δ), and the remaining candidates are omega (ω) wolves (Figure 4). Each wolf i moves towards the three leaders:

$$\mathbf{D}_\ell = |\mathbf{C}_\ell \circ \boldsymbol{\theta}_\ell - \boldsymbol{\theta}_i(t)|, \qquad \ell \in \{\alpha,\beta,\delta\} \tag{41}$$

$$\mathbf{X}_\ell = \boldsymbol{\theta}_\ell - \mathbf{A}_\ell \circ \mathbf{D}_\ell \tag{42}$$

$$\boldsymbol{\theta}_i(t+1) = \frac{\mathbf{X}_\alpha + \mathbf{X}_\beta + \mathbf{X}_\delta}{3} \tag{43}$$

with the coefficient vectors

$$\mathbf{A}_\ell = 2a\,\mathbf{r}_1 - a, \qquad \mathbf{C}_\ell = 2\,\mathbf{r}_2 \tag{44}$$

and the convergence parameter decreasing linearly over the iterations:

$$a(t) = 2\left(1 - \frac{t}{T_{\max}}\right) \tag{45}$$

The symbols are defined in Table 5. While $|A_{\ell,n}| > 1$, a wolf may move away from the leaders, which favours exploration of Θ. As a decreases, $|A_{\ell,n}| < 1$ and the pack converges towards the leaders (exploitation). GWO has only two algorithm-specific settings, N and $T_{\max}$, which simplifies its application compared with GA and

PSO. Like the other two methods, it has no general proof of global convergence.

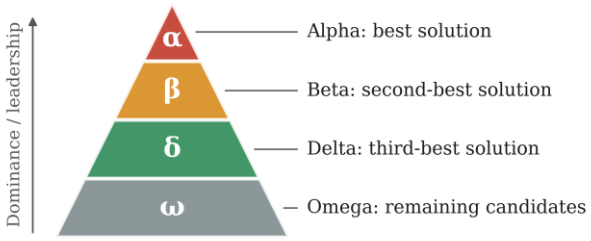

Fig. 4: Social hierarchy of the grey wolf pack used to rank candidate solutions in GWO.
Source: created by the author

Table 5. Notation of the Grey Wolf Optimizer

Symbol	Meaning
$\theta_i(t)$	Position of wolf i at iteration t (candidate gain vector)
θ_α, θ_β, θ_δ	Best, second-best and third-best solutions found so far
D_ℓ	Distance between wolf i and leader $\ell \in \{\alpha, \beta, \delta\}$
X_ℓ	Position suggested to wolf i by leader ℓ
A_ℓ	Coefficient vector controlling exploration ($\|A\| > 1$) and exploitation ($\|A\| < 1$)
C_ℓ	Random weighting of the leader position, in [0, 2]
a	Convergence parameter, decreasing linearly from 2 to 0
r_1, r_2	Random vectors with components uniform in [0, 1]
N, T_{max}	Number of wolves, maximum number of iterations

Source: created by the author

4.5 Evaluation Protocol

For a fair comparison, the three algorithms use the same population size N, the same number of iterations $T_{\max}$, the same bounds Θ, and the same fitness (36). Each algorithm therefore performs the same number of fitness evaluations, $N \times T_{\max}$, each requiring one simulation of the station model (Table 4). Because of this computational cost, each algorithm was run once. The convergence curves in Figure 8 therefore describe single realizations of the stochastic search. The comparison in Section 5 is therefore limited to the convergence behaviour and the final fitness of each run. A statistical study over multiple independent runs, and a station-level comparison of the resulting gain sets, are identified as future work.

5 Results and Discussions

5.1 MPPT Performance

Figure 5 shows the response of the two algorithms at a constant irradiance of 1000 W/m². Both reach the MPP (650.4 W) within about 20 ms. P&O settles slightly faster (16.0 ms against 18.8 ms). Once the MPP is reached, P&O keeps oscillating around it with a peak-to-peak ripple of 1.2 W (0.18 %), as shown in the zoomed view of Figure 5(c). INC holds the operating point with no measurable ripple.

Figure 6 and Figure 7 show the response to the irradiance steps. After each step, both algorithms recover the new MPP (516.3 W at 800 W/m² and 449.0 W at 700 W/m²) within 3 ms. In each new steady state, P&O again oscillates (1.3–1.6 W peak-to-peak), while INC remains at the MPP (at most 0.6 W ripple at 700 W/m²). Over the whole profile, the tracking efficiencies (31) are 99.63 % for P&O and 99.65 % for INC as shown in Table 6.

Table 6. MPPT performance of P&O and INC (650 W module)

Index	P&O	INC
Settling time (±2 %), 1000 W/m²	16.0 ms	18.8 ms
Ripple ΔP_{pp} at 1000 W/m²	1.2 W (0.18 %)	≈ 0 W
Ripple ΔP_{pp} at 800 / 700 W/m²	1.3 / 1.6 W	≈ 0 / 0.6 W
Recovery after 1000→800 W/m² step	2.8 ms	2.8 ms
Recovery after 800→700 W/m² step	2.5 ms	2.4 ms
η_{MPPT}, constant 1000 W/m²	99.72 %	99.75 %
η_{MPPT}, step profile (Figure 6)	99.63 %	99.65 %

Source: created by the author

The two algorithms therefore extract practically the same energy under uniform irradiance. The advantage of INC lies in eliminating the steady-state oscillation of the operating point, which reduces the ripple transmitted to the DC bus and the stress on the boost converter. For this reason, INC is used for both PV farms in the station simulations that follow.

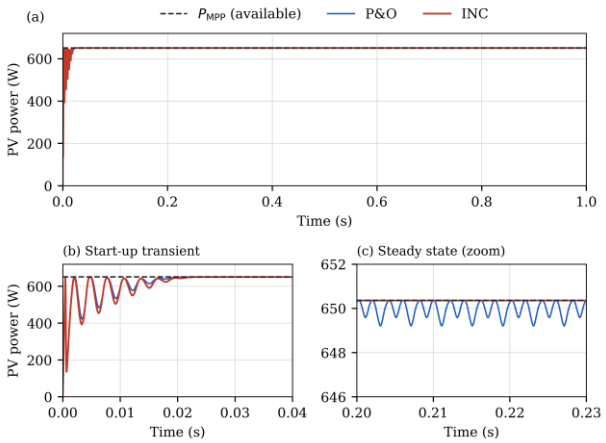

Fig. 5: P&O and INC tracking of a single 650 W module at 1000 W/m²: (a) full response, (b) start-up, (c) steady-state zoom
Source: created by the author

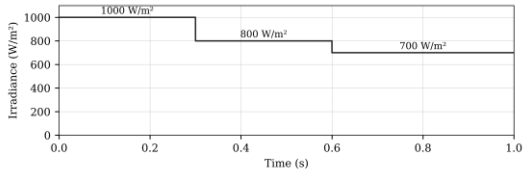

Fig. 6: Irradiance profile used in the dynamic MPPT test
Source: created by the author

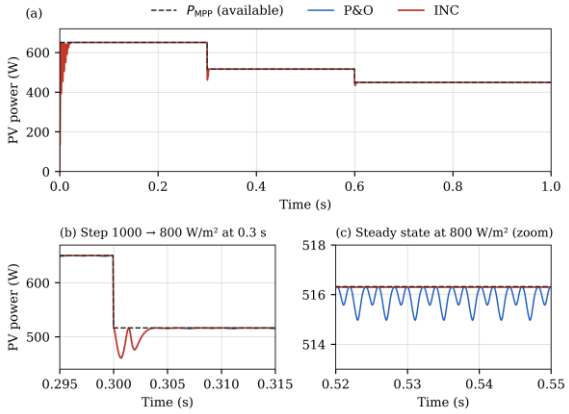

Fig.7: P&O and INC tracking under the irradiance profile of Figure 6: (a) full response, (b) step from 1000 to 800 W/m² at 0.3 s, (c) steady-state zoom at 800 W/m²
Source: created by the author

5.2 Controller Tuning Result

The PI gains were tuned with GA, PSO and GWO using the optimization problem of Section 4.1 and the settings of Table 5. Figure 8 shows the best fitness found at each iteration. GA improves its best solution gradually, in several discrete steps, and is still improving at the end of the 50 generations; over the run its best fitness decreases by 0.16 %. PSO and GWO both reach their final value early, at iteration 5 and iteration 4 respectively, and converge to the same best fitness, which is 0.08 % lower than the final GA value.

Within the common budget of $N \times T_{\max}$ fitness evaluations, PSO and GWO therefore locate a better solution than GA and need far fewer iterations to do so. GWO achieves this with only two algorithm-specific settings (N and $T_{\max}$), whereas PSO requires the inertia and acceleration coefficients of Table 5 to be chosen. The small relative spread of the final fitness values indicates that the three algorithms converge to neighbouring regions of the gain space. Because each algorithm was run once (Section 4.5), these differences describe single realizations of the stochastic search and are not claimed to be statistically significant.

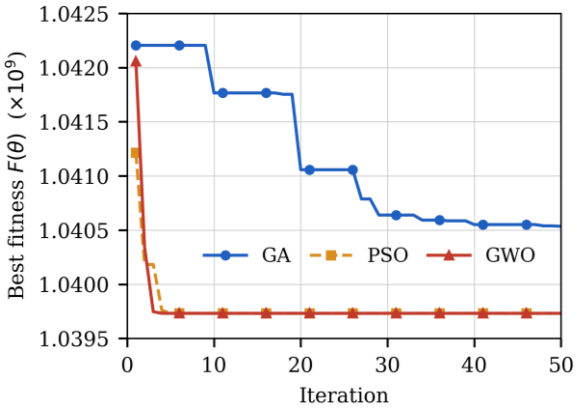

Fig. 8: Best fitness F(θ) (36) versus iteration for GA, PSO and GWO (single run per algorithm, N × T_{max} fitness evaluations)
Source: created by the author

6 Conclusion

This paper presented a modelling and controller-tuning framework for a grid-connected PV fast-charging station with a 1000 V DC bus, seven 80 kW chargers and a three-level NPC grid converter.

The main findings are as follows.

1. The station was described by an averaged, index-one differential-algebraic model with 47 states, whose solution exists and is unique between discrete events. The parameters impose a lower bound on the DC-bus voltage: the chargers need more than 830 V to regulate the battery in CV mode and the grid converter needs at least 816 V for linear modulation, so transient dips must stay below about 17 %. Because the DC link stores only 37.5 J, such dips develop within milliseconds, which makes

the DC-voltage loop the critical loop of the station.

2. P&O and INC MPPT achieved practically the same tracking efficiency (99.63 % and 99.65 % over the dynamic profile) and recovered from irradiance steps within 3 ms. P&O settled slightly faster at start-up (16.0 ms against 18.8 ms), whereas INC eliminated the steady-state power oscillation of P&O; INC was therefore selected for the station.
3. PI tuning was formulated as a constrained optimization problem with an explicit cost, operating-limit and stability constraints, and an existence argument for the optimal gains. In single runs with an identical evaluation budget, PSO and GWO reached the same best fitness within five iterations, while GA converged more slowly and ended 0.08 % higher. GWO required the fewest algorithm-specific settings.

The present results are limited to single optimization runs and to simulation. Future work will include a statistical comparison over multiple independent runs, a station-level comparison of the three optimized gain sets in terms of DC-bus voltage deviation, power delivery, conversion efficiency and harmonic distortion under EV load steps and CC/CV transitions, an eigenvalue-based verification of the stability margin of the tuned system, and hardware-in-the-loop validation.

Acknowledgement:
The author thankfully acknowledges the Power Electronics and Power Systems (PEPS) unit at Palestine Polytechnic University for its valuable support.

Declaration of Generative AI and AI-assisted Technologies in the Writing Process
During the preparation of this work, the author(s) utilized artificial intelligence (AI) technologies solely for the purpose of linguistic refinement and grammatical correction. Following the application of these tools, the author(s) comprehensively reviewed, verified, and edited the resulting text. The author(s) maintain full accountability and responsibility for the accuracy, integrity, and final content of the publication.

References:

[1] Barman, P., Dutta, L., Bordoloi, S., Kalita, A., Buragohain, P., Bharali, S., & Azzopardi, B., "Renewable energy integration with electric vehicle technology: A review of the existing smart charging approaches," *Renewable and Sustainable Energy Reviews*, 183, 2023. https://doi.org/10.1016/j.rser.2023.113518.

[2] Alrubaie, A. J., Salem, M., Yahya, K., Mohamed, M., & Kamarol, M., "A comprehensive review of electric vehicle charging stations with solar photovoltaic system considering market, technical requirements, network implications, and future challenges," *Sustainability*, 15, 2023. https://doi.org/10.3390/su15108122.

[3] Zentani, A., Almaktoof, A. M., & Kahn, M. T. E., "Exploring review of advancements in fast-charging techniques and infrastructure for electric vehicles revolution," *Energy Science & Engineering*, 13, 2025. https://doi.org/10.1002/ese3.70051.

[4] Chiradeja, P., Yoomak, S., Srisuksai, P., Klomjit, J., Ngaopitakkul, A., & Ananwattanaporn, S., "Development and analysis of a fast-charge EV-charging station model for power quality assessment in distribution systems," *Applied Sciences*, 15, 2025. https://doi.org/10.3390/app15179645.

[5] Ibrahim, M. H., Ang, S. P., Dani, M. N., Rahman, M. I., Petra, R., & Sulthan, S. M., "Optimizing step-size of perturb & observe and incremental conductance MPPT techniques using PSO for grid-tied PV system," *IEEE Access*, 11, 2023. https://doi.org/10.1109/ACCESS.2023.3242979.

[6] Mamizadeh, A., & Genc, N., "Performance analysis of meta-heuristic algorithms for optimal PI tuning of PFC," *Electric Power Components and Systems*, 52, 2024. https://doi.org/10.1080/15325008.2023.2291800.

[7] Gupta, M., Tiwari, P. M., Viral, R. K., Shrivastava, A., Abu Zneid, B., & Hunko, I., "Grid-connected PV inverter system control optimization using Grey Wolf optimized PID controller," *Scientific Reports*, 15, 2025. https://doi.org/10.1038/s41598-025-10617-7.

[8] Zaro, F., "Techno-economic sizing and optimization of a grid-connected photovoltaic electric vehicle charging station using HOMER: A case study of Palestine," *WSEAS Transactions on Circuits and Systems*, 25, 2026. https://doi.org/10.37394/23201.2026.25.27.

[9] Ridha, H. M., Hizam, H., Mirjalili, S., Othman, M. L., Ya'acob, M. E., & Ahmadipour, M., "Parameter extraction of single, double, and three diodes photovoltaic

model based on guaranteed convergence arithmetic optimization algorithm and modified third order Newton Raphson methods," *Renewable and Sustainable Energy Reviews*, 162, 2022. https://doi.org/10.1016/j.rser.2022.112436.

[10] Kilicoglu, H., & Tricoli, P., "Technical review and survey of future trends of power converters for fast-charging stations of electric vehicles," *Energies*, 16, 2023. https://doi.org/10.3390/en16135204.

[11] Ghaeminezhad, N., & Monfared, M., "Charging control strategies for lithium-ion battery packs: Review and recent developments," *IET Power Electronics*, 15, 2022. https://doi.org/10.1049/pel2.12219.

[12] Magdy, M., Hanafy, F., Abou-Zalam, B., & Nabil, E., "Optimized multi-stepped constant current constant voltage fast charging controller for lithium-ion batteries," *Scientific Reports*, 15, 2025. https://doi.org/10.1038/s41598-025-25924-2.

[13] Kishore, D. R., Muni, T. V., Raja, B. S., Pushkarna, M., Goud, B. S., AboRas, K. M., & Alphonse, S., "Grid-connected solar PV system with maximum power point tracking and battery energy storage integrated with sophisticated three-level NPC inverter," *International Transactions on Electrical Energy Systems*, 2023 (Article ID 3209485), 2023. https://doi.org/10.1155/2023/3209485.

[14] Zheng, Y., Han, Y., Wang, C., Ren, Q., Yang, P., & Zalhaf, A. S., "Impact of phase-locked loop on grid-connected inverter stability under weak grid conditions and suppression measures," *Computers and Electrical Engineering*, 123, 2025. https://doi.org/10.1016/j.compeleceng.2025.110249.

[15] Abssane, S., Outzourhit, A., & Amatoul, F. Z., "Comparison between incremental conductance and perturb and observe algorithms in photovoltaic system under low temperature and irradiation levels," *International Journal of Electrical and Computer Engineering*, 14, 2024. https://doi.org/10.11591/ijece.v14i5.pp4897-4906.

[16] Katoch, S., Chauhan, S. S., & Kumar, V., "A review on genetic algorithm: past, present, and future," *Multimedia Tools and Applications*, 80, 2021. https://doi.org/10.1007/s11042-020-10139-6.

[17] Shami, T. M., El-Saleh, A. A., Alswaitti, M., Al-Tashi, Q., Summakieh, M. A., & Mirjalili, S., "Particle swarm optimization: A comprehensive survey," *IEEE Access*, 10, 2022. https://doi.org/10.1109/ACCESS.2022.3142859.

[18] Zaro, F., & Altakrouri, S., "Optimal sizing and placement of distributed generators using multi-objective particle swarm optimization," *WSEAS Transactions on Power Systems*, 20, 2025. https://doi.org/10.37394/232016.2025.20.32.

[19] Liu, Y., As'arry, A., Hassan, M. K., Hairuddin, A. A., & Mohamad, H., "Review of the grey wolf optimization algorithm: variants and applications," *Neural Computing and Applications*, 36, 2024. https://doi.org/10.1007/s00521-023-09202-8.

[20] Nasir, M., Sadollah, A., Mirjalili, S., Mansouri, S. A., Safaraliev, M., & Rezaee Jordehi, A., "A comprehensive review on applications of grey wolf optimizer in energy systems," *Archives of Computational Methods in Engineering*, 32, 2025. https://doi.org/10.1007/s11831-024-10214-3.

Contribution of Individual Authors to the Creation of a Scientific Article (Ghostwriting Policy)

The author contributed in the present research, at all stages from the formulation of the problem to the final findings and solution.

Sources of Funding for Research Presented in a Scientific Article or Scientific Article Itself

No funding was received for conducting this study.

Conflict of Interest

The author has no conflicts of interest to declare that are relevant to the content of this article.

Creative Commons Attribution License 4.0 (Attribution 4.0 International, CC BY 4.0)

This article is published under the terms of the Creative Commons Attribution License 4.0
https://creativecommons.org/licenses/by/4.0/deed.en_US

APPENDIX

Table 1. System parameters of the proposed PV-based EV fast-charging station

Parameter	Value
PV plant	
PV module	650 W mono-crystalline PERC, 132 half-cut cells
V_{mp} / I_{mp}	37.9 V / 17.16 A
V_{oc} / I_{sc}	45.0 V / 18.39 A
Maximum system voltage	1500 V
String configuration	20 modules in series (V_{mp} = 758 V, V_{oc} = 900 V)
PV farm 1	77 strings, 1,540 modules, 1.00 MW
PV farm 2	58 strings, 1,160 modules, 0.754 MW
Total PV capacity	2,700 modules, 1.755 MW (STC)
DC–DC stage	
Converter	One boost converter per PV farm
MPPT algorithm	Incremental Conductance (INC)
Duty cycle at STC	≈ 0.24 (758 V → 1000 V)
DC bus	
DC-bus voltage	1000 V
DC-link capacitors	2 × 150 µF (split DC link)
Grid-side converter	
Topology	Three-level NPC VSC, bidirectional
Rated power	2.25 MVA
AC voltage / frequency	500 V (rms, line-to-line) / 50 Hz
Output filter	L = 44.2 µH, R = 1 mΩ
Switching frequency	40 kHz
Control sampling time	25 µs
Grid interface	
Step-up transformer	0.5 / 11 kV
Utility grid	11 kV, 50 Hz
EV charging units	
Number / rating	7 × 80 kW (560 kW total)
Charger converter	Buck DC–DC, PI-controlled CC/CV
EV battery	Li-ion, 800 V nominal, 62.5 Ah (50 kWh)
CC stage	100 A (1.6C) up to SoC = 80%
CV stage	830 V
Parameter	**Value**
Simulation	
Platform / solver	MATLAB/Simulink, discrete, 5 µs step

Source: created by the author